

## Discovery of Raman-scattered He II $\lambda 6545$ in the Planetary Nebulae NGC 6886 and NGC 6881

BO-EUN CHOI <sup>1</sup> AND HEE-WON LEE <sup>1</sup>

<sup>1</sup>*Department of Physics and Astronomy, Sejong University, Seoul, Korea*

(Received June 1, 2019; Revised September 23, 2020; Accepted October 26, 2020)

Submitted to ApJL

### ABSTRACT

Young planetary nebulae (PNe) retain a large amount of neutral material that was shed in the previous asymptotic giant branch stage. The thick H I region in young PNe can be effectively probed by illuminating far UV radiation that may be inelastically scattered to appear in the optical region. Raman-scattered features are unique spectroscopic tracers of neutral regions that can be used to investigate the mass-loss process in young PNe. We conduct high resolution spectroscopy of young PNe using BOES (the Bohyunsan Observatory Echelle Spectrograph) and report the discovery of a Raman-scattered He II feature at 6545 Å in NGC 6886 and NGC 6881. The Raman-scattered He II features have been found in only five PNe so far, and, in particular, it is the first direct detection of an H I component in NGC 6881. The Raman He II  $\lambda 6545$  features in the two PNe are observed to be redshifted with respect to He II  $\lambda 6560$ , indicating that the neutral regions are expanding. We perform line profile analyses using the grid-based Monte Carlo code ‘STaRS’ by assuming a neutral hydrogen region in the shape of a partial spherical shell expanding radially. The profiles are well fitted with the model parameters of covering factor  $CF = 0.3$ , H I column density  $N_{\text{HI}} = 5 \times 10^{20} \text{ cm}^{-2}$ , and expansion speed  $v_{\text{exp}} = 25 \text{ km s}^{-1}$  for NGC 6886 and  $CF = 0.6$ ,  $N_{\text{HI}} = 3 \times 10^{20} \text{ cm}^{-2}$ , and  $v_{\text{exp}} = 30 \text{ km s}^{-1}$  for NGC 6881, respectively.

*Keywords:* line: formation — planetary nebulae: general — planetary nebulae: individual (NGC 6881, NGC 6886) — scattering — stars: mass-loss

### 1. INTRODUCTION

Low and intermediate mass stars ( $0.8 - 8 M_{\odot}$ ) lose a significant fraction of their mass through slow stellar winds in the asymptotic giant branch (AGB) stage, which plays a crucial role in the chemical enrichment of the interstellar medium (Kwok 2005; Höfner & Olofsson 2018). The hot core part evolves into a white dwarf with a mass less than the Chandrasekhar limit ( $M_{\text{WD}} < 1.4 M_{\odot}$ ), and the ejected material forms a planetary nebula (PN). A young PN is an ionization-bounded system which contains both ionized and neutral regions (Dinerstein 1991; Webster et al. 1988; Taylor, Gussie & Pottasch 1990; Kastner et al. 1996; Huggins et al. 2005; Guzman-Ramirez et al. 2018). Because young PNe have recently entered into the PN stage, they are

ideal objects to investigate the mass-loss history in the late stage of stellar evolution.

The existence of an H I component in PNe is known, but still not well understood. One possibility for the existence of an H I component is left over from the previous AGB stage (Glassgold & Huggins 1983). Another possibility is that the atomic hydrogen component is formed by the photodissociation of H<sub>2</sub>. H I provides important information about the outer region of the circumstellar envelope (CSE) and the interaction between the CSE and interstellar medium (Matthews et al. 2013). Although atomic components are difficult to investigate due to severe confusion from the Galactic emission, successful H I 21 cm observations have been carried out, resulting in successful detections of H I regions with mass  $\sim 0.01 M_{\odot}$  in a number of young PNe (Taylor, Gussie & Pottasch 1990; Gussie & Taylor 1995).

Another useful tool to probe the thick neutral region is Raman-scattered emission line features formed via

the inelastic scattering of far-UV photons by hydrogen atoms. When a far-UV photon with energy near  $\text{Ly}\beta$  is incident on a hydrogen atom, an optical photon near  $\text{H}\alpha$  can be emitted if the hydrogen atom de-excites into the  $2s$  state instead of the ground state. Raman scattering with atomic hydrogen as an astrophysical tool was first suggested by Schmid (1989). He identified the broad emission features at 6830 Å and 7088 Å in symbiotic stars as Raman-scattered features of O VI  $\lambda\lambda 1032$  and 1038 (Allen 1980; Akras et al. 2019). Symbiotic stars are wide binary systems consisting of an accreting white dwarf and a mass losing giant. They provide an ideal place to observe Raman scattering because of the copious amount of far UV photons emanating from the vicinity of the white dwarf. These UV photons are incident on a thick neutral hydrogen region formed around the evolved giant. Nussbaumer, Schmid & Vogel (1989) proposed that photons from He II can be Raman-scattered with hydrogen atoms producing emission lines that can be observed. These Raman-scattered He II features have been detected in the symbiotic stars RR Telescopii, V1016 Cygni, HM Sagittae, and V835 Centauri (van Groningen 1993; Lee, Kang & Byun 2001; Birriel 2004).

Strong He II emitters are found amongst young PNe having a central star still sufficiently hot to ionize He II with a thick atomic hydrogen component ejected in the previous AGB stage. Raman-scattered He II  $\lambda 6545$  was reported to be found in the young PNe NGC 7027, IC 5117, and NGC 6790 (Péquignot, Walsh & Morisset 2003; Lee et al. 2006; Kang, Lee & Lee 2009). The detection of Raman-scattered He II  $\lambda 4851$  arising from Raman scattering of He II  $\lambda 972$  was reported in the PNe NGC 7027, NGC 6302, NGC 6886, and IC 5117 (Péquignot et al. 1997; Groves et al. 2002; Péquignot, Walsh & Morisset 2003; Lee et al. 2006).

In this paper, we report our first detection of Raman-scattered He II  $\lambda 6545$  in the two young PNe NGC 6886 and NGC 6881.

## 2. ATOMIC PHYSICS

Raman scattering of atomic hydrogen with incident far UV radiation near the Lyman  $n \rightarrow 1$  ( $n \geq 3$ ) series may result in the emission of an optical photon near the Balmer  $n \rightarrow 2$  series. The wavelength of Raman-scattered radiation ( $\lambda_o$ ) is related to that of the incident radiation ( $\lambda_i$ ) by energy conservation:

$$\lambda_o^{-1} = \lambda_i^{-1} - \lambda_{\text{Ly}\alpha}^{-1}, \quad (1)$$

where  $\lambda_{\text{Ly}\alpha}$  is the wavelength of  $\text{Ly}\alpha$ . He II and H I are single electron systems, sharing the same electronic level structure. The level spacing of He II is larger than

that of H I by a factor slightly exceeding 4 augmented by the fact that the two body reduced mass of He II is larger by a factor  $\sim 3m_e/4m_p$ , where  $m_e$  and  $m_p$  are the electron and proton masses. This leads to the far UV He II ( $2n \rightarrow 2$ ) line being systematically blueshifted by an amount  $\sim -120 \text{ km s}^{-1}$  compared to the H I ( $n \rightarrow 1$ ) Lyman line (Lee, Kang & Byun 2001). In particular, He II  $\lambda 1025$  ( $n = 4 \rightarrow 2$ ) is Raman-scattered to form an optical feature at 6545 Å according to Eq. (1). In addition, Raman scattering He II  $\lambda 972$  ( $n = 6 \rightarrow 2$ ) may form an optical feature at 4851 Å.

Differentiation of Eq. (1) yields the relation between the line widths ( $\Delta\lambda_o$  and  $\Delta\lambda_i$ ):

$$\frac{\Delta\lambda_o}{\lambda_o} = \left(\frac{\lambda_o}{\lambda_i}\right) \frac{\Delta\lambda_i}{\lambda_i}, \quad (2)$$

giving rise to the formation of broad Raman-scattered features by a factor  $\lambda_o/\lambda_i$ . In the case of Raman scattering near  $\text{Ly}\beta$ , this factor is  $\sim 6.4$ . This means that a far UV line with a line width  $\Delta v = 30 \text{ km s}^{-1}$  may form a Raman feature with a significantly broadened width of  $\sim 190 \text{ km s}^{-1}$ .

Cross sections for Rayleigh and Raman scattering are computed using time dependent second order perturbation theory (e.g., Nussbaumer, Schmid & Vogel 1989; Lee et al. 2006). In particular, the cross sections for Rayleigh and Raman scattering of He II  $\lambda 1025$  are  $\sim 5.7 \times 10^{-21} \text{ cm}^2$  and  $\sim 7.4 \times 10^{-22} \text{ cm}^2$ , respectively. Raman He II at 6545 Å becomes an excellent probe of H I regions characterized by the H I column density  $N_{\text{HI}}$  in excess of  $10^{20} \text{ cm}^{-2}$ .

## 3. SPECTROSCOPY OF PLANETARY NEBULAE

### 3.1. Observation

Based on the He II  $\lambda 4686$  line intensity catalog of PNe compiled by Tyllenda et al. (1994), we selected candidates with the first priority given to strong He II emitters, for which the line intensity ratio between  $\text{H}\alpha$  and He II  $\lambda 4686$ ,  $I(\text{HeII}4686)/I(\text{H}\alpha) \gtrsim 0.05$ . We also included the young PNe investigated by Sahai, Morris & Villar (2011), since they are considered to possess much neutral matter including atomic hydrogen despite a relatively low value of  $I(\text{HeII}4686)/I(\text{H}\alpha)$ .

We performed high resolution spectroscopy for 12 PNe during April 2019 - March 2020 using the Bohyunsan Observatory Echelle Spectrograph (BOES) on the 1.8 m telescope at Bohyunsan Optical Astronomy Observatory (BOAO). BOES is an optical fiber-fed echelle spectrograph with a wide spectral coverage of 3500-10500 Å encompassing the entire optical wavelength range. The resolution and the field of view of the spectrograph depends on the diameter of the optical fiber connected to

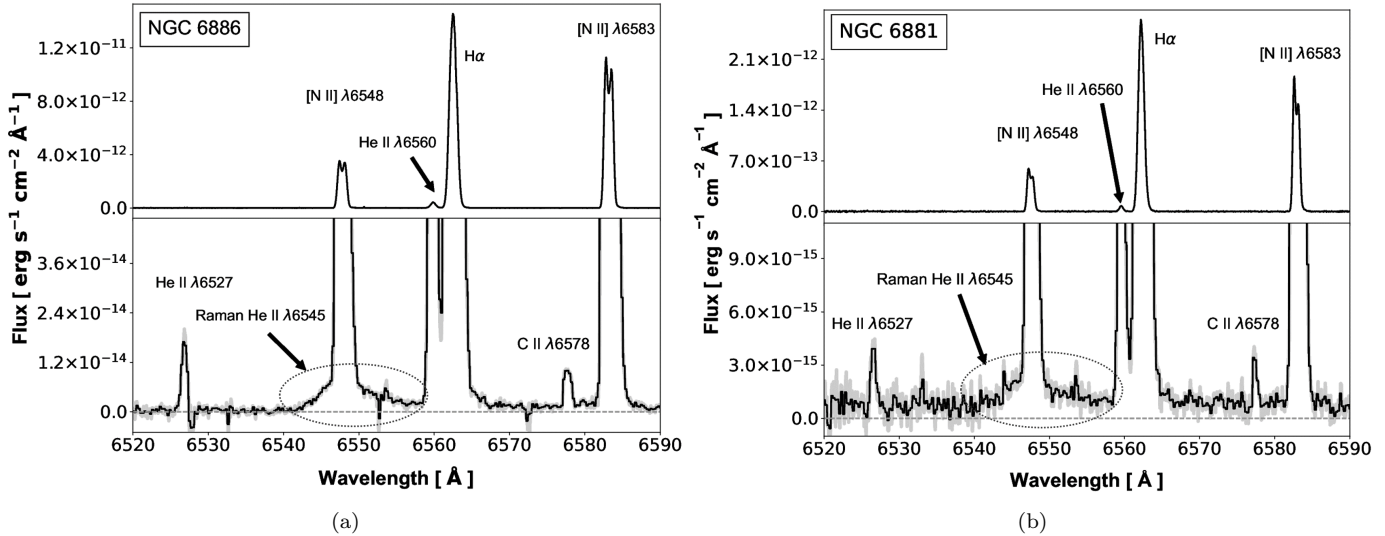


**Figure 1.** High-resolution spectra of NGC 6886 (left) and NGC 6881 (right) obtained using BOES. We present raw data (gray) and rebinned data (black). Upper panels show the short exposure spectra to present strong emission lines including H $\alpha$ , He II, and [N II] lines. Lower panels show the long exposure spectra rescaled for clear presentation of weak lines He II  $\lambda$ 6527, C II  $\lambda$ 6578. The broad wing-like feature near [N II]  $\lambda$ 6548 is the Raman-scattered He II  $\lambda$ 6545 line, and has been denoted by a circle.

it. A narrower optical fiber gives higher resolution but a smaller field of view and vice versa. Our observations were carried out using a fiber having a spectral resolution of  $R \sim 30,000$  and a field of view of  $4.2''$ . To improve the signal-to-noise ratio,  $2 \times 2$  binning was applied at the expense of spectral resolution. Both short and long exposures were taken for each target because Raman-scattered He II features are very weak with a line flux about  $10^{-3}$  times that of H $\alpha$ .

The data were reduced using IRAF<sup>1</sup>. Image preprocessing was carried out using bias and dome flat images. Spectra of a ThAr lamp were obtained for wavelength calibration. Flux calibration was carried out using the spectrophotometric standard stars HR 3454, HR 4554, HR 5501, and HR 9087.

### 3.2. Spectra of NGC 6886 and NGC 6881

While there were several marginal detections of the Raman-scattered He II features, here we present the two most clear detections. These sources were NGC 6886 and NGC 6881. The left and right panels of Fig. 1 show the BOES spectra of NGC 6886 and NGC 6881, respectively. The upper and lower panels show the short and long exposure spectra, respectively. Total integrated times for the long exposure were 2,400 and 3,300 seconds

for NGC 6886 and NGC 6881, respectively. Strong emission lines including H $\alpha$ , He II  $\lambda$ 6560 and [N II]  $\lambda$ 6548 and 6583 are found in the upper panels.

In the lower panels, there appear clearly two weak emission lines He II  $\lambda$ 6527 and C II  $\lambda$ 6578. There are broad emission features seen in both sources (denoted with circles) which are blended with [N II]  $\lambda$ 6548. These are the Raman-scattered He II lines at 6545 Å. Despite the [N II]  $\lambda$ 6583 line being theoretically 3 times stronger than [N II]  $\lambda$ 6548, the absence of a broad emission feature around the [N II]  $\lambda$ 6583 line means we are confident in our identification of the Raman-scattered He II lines. Furthermore, case B recombination theory predicts that the peak value of He II  $\lambda$ 6527 is comparable to that of the Raman-scattered He II  $\lambda$ 6545, which can be seen in Fig. 1 (Storey & Hummer 1995; Lee et al. 2006).

The profiles of strong lines H $\alpha$  and He II  $\lambda$ 6560 shown in the upper panels are fairly symmetric. However, it is apparent that the Raman He II features exhibit an extended red tail. Although severe blending with [N II]  $\lambda$ 6548 hinders quantitative analyses, as a first approximation to the line profiles, we applied a single Gaussian fitting to each of the H $\alpha$ , He II, and Raman He II  $\lambda$ 6545 lines. The results are presented in Table 1. Here,  $\lambda_c$  is observed center wavelength of each emission line, and  $f_0$  is the peak value of line flux. The full width at half maximum (FWHM) in velocity space is represented by  $v_G$ .

The line center of Raman He II  $\lambda$ 6545 is expected to be found at 6544.47 Å for NGC 6886 and at 6542.76 Å for

<sup>1</sup> IRAF is distributed by the National Optical Astronomy Observatories, which are operated by the Association of Universities for Research in Astronomy, Inc., under cooperative agreement with the National Science Foundation.

PN	Line	$\lambda_c$ (Å)	$f_0$ ( $\text{erg s}^{-1}\text{cm}^{-2}\text{Å}^{-1}$ )	$v_G$ ( $\text{km s}^{-1}$ )
NGC 6886	H $\alpha$	6562.51	$1.47 \times 10^{-11}$	50
	He II $\lambda 6560$	6559.84	$4.29 \times 10^{-13}$	36
	He II $\lambda 6527$	6526.78	$1.96 \times 10^{-14}$	36
	Raman He II	6548.65	$7.31 \times 10^{-15}$	412
NGC 6881	H $\alpha$	6562.23	$3.18 \times 10^{-12}$	34
	He II $\lambda 6560$	6559.57	$9.04 \times 10^{-14}$	29
	He II $\lambda 6527$	6526.63	$4.02 \times 10^{-15}$	29
	Raman He II	6547.93	$2.05 \times 10^{-15}$	379

**Table 1.** Single Gaussian parameters for H $\alpha$ , He II emission lines, and Raman He II  $\lambda 6545$  feature of NGC 6886 and NGC 6881 spectra.

NGC 6881 based on the values of  $\lambda_c$  of He II  $\lambda 6560$  and the atomic physical relation given by Eq. (1). However, considerable redward deviations of  $\sim +190 \text{ km s}^{-1}$  and  $\sim +240 \text{ km s}^{-1}$  are found for NGC 6886 and NGC 6881, respectively. Considering the line broadening effect of Raman scattering described by Eq. (2), these deviations correspond to receding motions of the H I region with  $\sim 30 \text{ km s}^{-1}$  and  $\sim 40 \text{ km s}^{-1}$  with respect to the central far UV He II emission region in NGC 6886 and NGC 6881, respectively.

The He II emission lines are observed to be narrower than H $\alpha$  with  $v_G \sim 36 \text{ km s}^{-1}$  for NGC 6886 and  $29 \text{ km s}^{-1}$  for NGC 6881, respectively. If the Raman conversion efficiency is independent of wavelength, then we may expect that the Raman He II  $\lambda 6545$  features have the line widths of  $v_G \sim 200 \text{ km s}^{-1}$ , which is much smaller than the values  $\sim 400 \text{ km s}^{-1}$  shown in Table 1. However, the sharply increasing cross section across the He II  $\lambda 1025$  line implies that the Raman conversion efficiency increases toward the red part. This leads to the resultant line profiles of Raman He II that are significantly enhanced in the red part with additional line broadening (Choi et al. 2020).

#### 4. LINE FORMATION OF RAMAN-SCATTERED HE II

Choi et al. (2020) performed an extensive study of line formation of Raman He II in an expanding H I region with a constant speed by carrying out grid-based Monte Carlo simulations. They showed that complicated behavior manifests itself as center shifts, significant distortions of the line profile, and the appearance of a secondary peak when the H I region expands with a typical speed of  $\sim 30 \text{ km s}^{-1}$ .

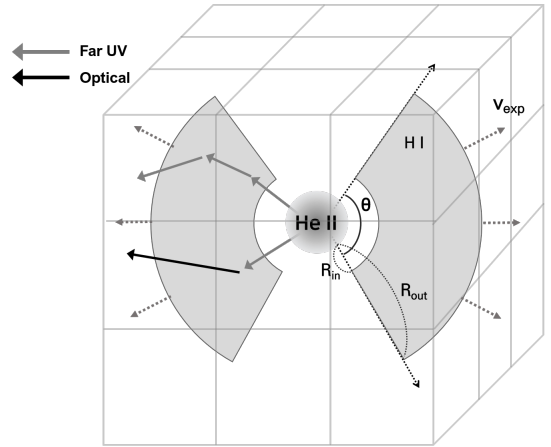


**Figure 2.** Schematic illustration of the simulation. The neutral region is assumed to be a partial spherical shell with the inner and outer radii  $R_{in}$  and  $R_{out}$ , respectively, and the opening angle  $\theta$ . The scattering region is divided into a large number of small cubical grids to trace each photon until escape.

The same grid-based Monte Carlo code ‘STaRS<sup>2</sup>’ is used to investigate the distribution and kinematics of the neutral hydrogen regions in NGC 6886 and NGC 6881. Fig. 2 shows a schematic illustration of the scattering geometry adopted in this work. The scattering region is a partial spherical shell surrounding the central He II region. The covering factor  $CF$  is defined as  $CF = \frac{\theta}{\pi}$ , where  $\theta$  is the opening angle of the partial spherical shell. The H I region is assumed to be of uniform density expanding with a single speed  $v_{exp}$ .

Far UV He II  $\lambda 1025$  photons generated in the central He II region are incident on the H I region. The neutral region is optically thick to Rayleigh-scattered UV photons, and optically thin to Raman-scattered optical photons. Each far UV photon is traced until escape from the neutral region through multiple Rayleigh scattering, or after Raman scattering. The incident far UV He II  $\lambda 1025$  is assumed to be described by a single Gaussian function determined in Section 3.2.

A simulation model is set with the following free parameters: the covering factor  $CF$  of the scattering region, H I column density  $N_{HI}$ , and expanding speed  $v_{exp}$ . The incident He II  $\lambda 1025$  flux is deduced from the observed He II  $\lambda 6560$  line flux and using case B recombination theory (Storey & Hummer 1995). We refer to Hyung, Keyes & Aller (1995) and Pottasch & Surendiranath (2005) for NGC 6886 and also Kaler, Pratap & Kwitter (1987) for NGC 6881 for the values of  $T_e = 1.25 \times 10^4 \text{ K}$  and  $n_e = 10^4 \text{ cm}^{-3}$ .

<sup>2</sup> <http://github.com/csj607/STaRS>



In Fig. 3, we present our best-fit results for NGC 6886 and NGC 6881 in the middle panels. The gray lines represent the observational data and the black lines show our best-fit simulation results. Despite severe blending of the Raman-scattered He II features with strong [N II]  $\lambda 6548$  lines, the broad features with a red tail structure are conspicuous in both PNe. These red-tailed features are attributed to the expansion of H I region.

In the case of NGC 6886, the best-fit model parameters are  $CF = 0.3$ ,  $N_{\text{HI}} = 5 \times 10^{20} \text{ cm}^{-2}$ , and  $v_{\text{exp}} = 25 \text{ km s}^{-1}$  (CF30-N5E20-V25). Similarly for NGC 6881, the best-fit model is found with parameters of  $CF = 0.6$ ,  $N_{\text{HI}} = 3 \times 10^{20} \text{ cm}^{-2}$ , and  $v_{\text{exp}} = 30 \text{ km s}^{-1}$  (CF60-N3E20-V30). The line flux of Raman He II is mainly determined by the product of the covering factor  $CF$  and H I column density  $N_{\text{HI}}$ , resulting in degeneracy in the modeling of Raman He II. However, it appears that the fit to Raman He II  $\lambda 6545$  becomes better with a somewhat lower covering factor  $CF < 0.5$  for NGC 6886 and a higher value  $CF > 0.5$  for NGC 6881, respectively.

In Fig. 3, the models with a lower expansion speed (top panels) and a higher speed (bottom panels) show significantly poorer fit to the observed data, providing valid ranges of  $v_{\text{exp}} = 25 \pm 5 \text{ km s}^{-1}$  for NGC 6886 and  $v_{\text{exp}} = 30 \pm 10 \text{ km s}^{-1}$  for NGC 6881, respectively. However, the insufficient data quality and severe blending with [N II] prevent us from putting strong constraints on the model parameters.

## 5. SUMMARY AND DISCUSSION

We report our successful detection of Raman-scattered He II at  $6545 \text{ \AA}$  in two young planetary nebulae NGC 6886 and NGC 6881. Gaussian model fitting is applied to find that the H $\alpha$  and He II  $\lambda 6560$  lines are symmetric whereas the Raman-scattered He II features appear redshifted from their expected atomic line center and exhibit an extended red tail structure indicative of the expanding H I regions with respect to the hot central emission region. We perform Monte Carlo simulations using the grid-based 3D code ‘STaRS’ to obtain best fitting profiles.

In the case of NGC 6886, Péquignot, Walsh & Morisset (2003) mentioned their detection of Raman-scattered He II at  $4851 \text{ \AA}$  blueward of H $\beta$ . Our best fit models suggest that the column density of atomic hydrogen region  $N_{\text{HI}} \sim 5 \times 10^{20} \text{ cm}^{-2}$  with its covering factor  $CF \sim 0.3$ . We also measure its expanding speed  $v_{\text{exp}} = 25 \text{ km s}^{-1}$ . A similar result was reported by Taylor, Gussie & Pottasch (1990).

On the other hand, it is the first direct detection of an H I component in NGC 6881. NGC 6881 is an interesting object exhibiting highly collimated quadrupo-

lar lobes and a multiple ring structure of the ionized region that is attributed to a precessing jet (Guerrero & Manchado 1998; Kwok & Su 2005). Furthermore, Ramos-Larios, Guerrero & Miranda (2008) argued that its ionized quadrupolar lobes and H<sub>2</sub> bipolar lobes show different morphologies and collimation degrees, indicating that this system underwent multiple bipolar ejections with varying mechanisms. We estimate the H I column density  $N_{\text{HI}} \sim 3 \times 10^{20} \text{ cm}^{-2}$  and the expansion speed  $v_{\text{exp}} = 30 \text{ km s}^{-1}$  assuming a covering factor of  $CF \sim 0.6$ .

The total H I mass  $M_{\text{HI}}$  based on our model is given by

$$M_{\text{HI}} \simeq 1.4 \times 10^{-4} \left( \frac{N_{\text{HI}}}{10^{20} \text{ cm}^{-2}} \right) \left( \frac{R_{\text{out}}}{10^3 \text{ au}} \right)^2 CF M_{\odot}, \quad (3)$$

where we set  $R_{\text{out}}$  to 2 times of  $R_{\text{in}}$ . The distance to NGC 6886 is about 2.6 kpc and the angular size of its central ionized region as measured from its optical image is roughly  $5''$  (Pottasch & Surendiranath 2005) (assumed to be  $R_{\text{in}}$ ), corresponding to a linear size of 13,000 au. This leads to an estimate of  $M_{\text{HI}} \sim 0.03 M_{\odot}$ . The distance to NGC 6881 is  $\sim 2.5$  kpc (Cahn, Kaler & Stanghellini 1992) with an angular size of its central ionized region being  $\sim 5''$  (Kwok & Su 2005), corresponding to a linear size of 13,000 au and therefore  $M_{\text{HI}} \sim 0.04 M_{\odot}$ . Setting  $R_{\text{out}}$  to be twice  $R_{\text{in}}$  is somewhat arbitrary and of course if we set  $R_{\text{out}}$  to be 4 times  $R_{\text{in}}$ , then the H I mass estimate will increase by 4 times.

Raman-scattered He II features can be formed near the hydrogen Balmer series at  $6545 \text{ \AA}$ ,  $4851 \text{ \AA}$ , and  $4332 \text{ \AA}$  derived from Raman scattering of far UV He II  $\lambda 1025$ ,  $\lambda 972$ , and  $\lambda 949$ , respectively. The integrated line analyses of Raman He II features are an appropriate probe of H I regions with a column density of  $N_{\text{HI}} \sim 10^{20-23} \text{ cm}^{-2}$ . Deep spectroscopy is required to detect Raman He II  $\lambda \lambda 4851$  and  $4332$ . The detection of these lines will allow us to carry out better studies of the kinematics and distribution of thick neutral hydrogen regions in PNe.

It is notable that both Raman He II features and C II  $\lambda 6578$  in emission is detected in NGC 7027, IC 5117, NGC 6790, similar to our two targets NGC 6886 and NGC 6881 (Keyes, Aller & Feibelman 1990; Lee et al. 2006; Kang, Lee & Lee 2009). Furthermore, these objects are also strong polycyclic aromatic hydrocarbon (PAH) emitters (Smith & McLean 2008; Ohsawa et al. 2016) indicating that these PNe possess carbon enriched environments from the previous AGB stage as a result of dredge-up processes. However, due to small number statistics it is too early to conclude that Raman-scattered He II features are found in only carbon en-

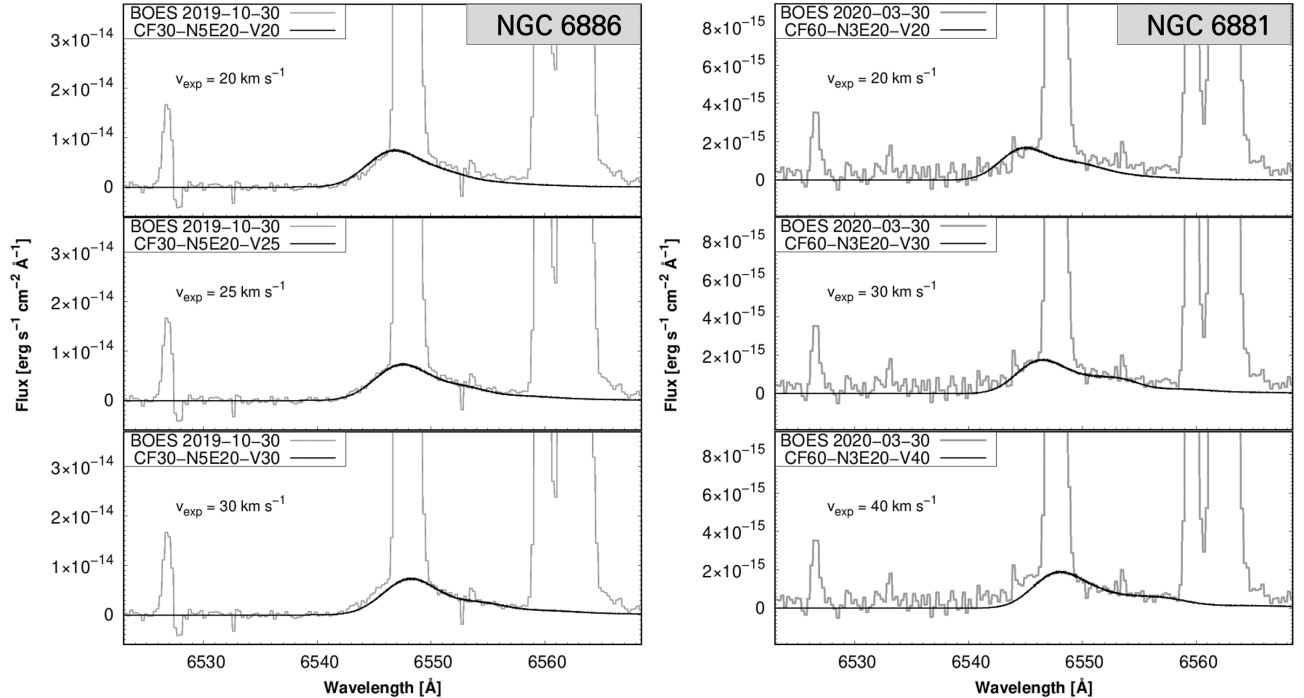


**Figure 3.** Comparison of the observational data (gray) and our simulation data (black) for NGC 6886 (left) and NGC 6881 (right). The best-fit models are found in the middle panels. In the middle-left panel, the model parameters are  $CF = 0.3$ ,  $N_{\text{HI}} = 5 \times 10^{20} \text{ cm}^{-2}$ , and  $v_{\text{exp}} = 25 \text{ km s}^{-1}$  (CF30-N5E20-V25). We also present models with a lower expansion speed of  $v_{\text{exp}} = 20 \text{ km s}^{-1}$  (CF30-N5E20-V20, top-left) and a higher value of  $30 \text{ km s}^{-1}$  (CF30-N520-V30, bottom-left) for comparison. In the middle-right panel, the model parameters are  $CF = 0.6$ ,  $N_{\text{HI}} = 2 \times 10^{20} \text{ cm}^{-2}$ , and  $v_{\text{exp}} = 30 \text{ km s}^{-1}$  (CF60-N3E20-V30). The top-right and bottom-right panels show the models with  $v_{\text{exp}} = 20 \text{ km s}^{-1}$  (CF60-N3E20-V20) and  $40 \text{ km s}^{-1}$  (CF60-N3E20-V40), respectively.

riched PNe. A definite conclusion should wait for a more systematic survey of PNe with Raman-scattered He II.

#### ACKNOWLEDGMENTS

The authors are grateful to the staff of the BOAO and Seulgi Kim for her help in the data acquisition of NGC 6886. This research was supported by the Korea Astronomy and Space Science Institute under the R&D program (Project No. 2018-1-860-00) supervised by the Ministry of Science, ICT and Future Planning. This work was also supported by a National Research Foundation of Korea (NRF) grant funded by the Korea government (MSIT: No. NRF-2018R1D1A1B07043944).

#### REFERENCES

- Akras, S., Guzman-Ramirez, L., Leal-Ferreira, M. L. & Ramos-Larios, G. 2019, *ApJS*, 240, 21
- Allen, D. A. 1980, *MNRAS*, 190, 75
- Birriel, J. J. 2004, *ApJ*, 612, 1136
- Cahn, J. H., Kaler, J. B. & Stanghellini, L. 1992, *A&AS*, 94, 399
- Choi, B.-E., Chang, S.-J., Lee, H.-G. & Lee, H.-W. 2020, *ApJ*, 889, 2
- Dinerstein, H. L. 1991, *PASP*, 103, 861
- Glassgold, A. E. & Huggins, P. J. 1983, *MNRAS*, 203, 517
- Groves, B., Dopita, M., Williams, R., et al. 2002, *PASA*, 19, 425

- Guerrero, M. A. & Manchado, A. 1998, *ApJ*, 508, 262
- Gussie, G. T. & Taylor, A. R. 1995, *MNRAS*, 273, 790
- Guzman-Ramirez, L., Gómez-Ruíz, A. I., Boffin, H. M. J., et al. 2018, *A&A*, 618, 91
- Höfner, S. & Olofsson, H. 2018, *A&A Rv*, 26, 1
- Huggins, P. J., Bachiller, R., Planesas, P., et al. 2005, *ApJS*, 160, 272
- Hyung, S., Keyes, C. D. & Aller, L. H. 1995, *MNRAS*, 272, 49
- Kaler, J. B., Pratap, P. & Kwitter, K. B. 1987, *PASP*, 99, 952
- Kang, E.-H., Lee, B.-C., & Lee, H.-W. 2009, *ApJ*, 695, 542
- Kastner, J. H., Weintraub, D. A., Gatley, I., et al. 1996, *ApJ*, 462, 777
- Keyes, C. D., Aller, L. H. & Feibelman, W. A. 1990, *PASP*, 102, 59
- Kwok, S. 2005, *JKAS*, 39, 271
- Kwok, S. & Su, K. Y. L. 2005, *ApJL*, 635, 49
- Lee, H.-W., Jung, Y.-C., Song, I.-O., et al. 2006, *ApJ*, 636, 1045
- Lee, H.-W., Kang, Y.-W. & Byun, Y.-I. 2001, *ApJ*, 211, 121
- Matthews, L. D., Le Bertre, T., Gérard & Johnson, M. C. 2013, *AJ*, 145, 97
- Nussbaumer, H., Schmid, H. M. & Vogel, M. 1989, *A&A*, 211, 27
- Ohsawa, R., Onaka, T., Sakon, I., et al. 2016, *AJ*, 151, 93
- Péquignot, D., Baluteau, J., Morisset, C., et al. 1997, *A&A*, 222, 217
- Péquignot, D., Walsh, J. R. & Morisset, C. 2003, *IAUS*, 209, 403
- Pottasch, S. R. & Surendiranath, R. 2005, *A&A*, 432, 139
- Ramos-Larios, G., Guerrero, M. A. & Miranda L. F. 2008, *AJ*, 135, 1441
- Sahai, R., Morris, M. R. & Villar, G. G. 2011, *AJ*, 141, 134
- Schmid, H. M. 1989, *A&A*, 211, 31
- Smith, E. C. D. & McLean, I. S. 2008, *ApJ*, 676, 408
- Storey, P. J. & Hummer, D. G. 1995, *MNRAS*, 272, 41
- Taylor, A. R., Gussie, G. T. & Pottasch, S. R. 1990, *ApJ*, 351, 515
- Tylenda, R., Stasińska, G., Acker, A. & Stenholm, B. 1994, *A&AS*, 106, 559
- van Groningen, E. 1993, *MNRAS*, 264, 975
- Webster, B. L., Payne, P. W., Storey, J. W. V. & Dopita, M. A., 1988, *MNRAS*, 235, 533